New results on proton-induced reactions on vanadium for ^{47}Sc production and the impact of level densities on theoretical cross sections

F. Barbaro,[1,2] L. Canton,[1] M. P. Carante,[2,3] A. Colombi,[2,3] L. De Dominicis,[4,5] A. Fontana,[3] F. Haddad,[6,7] L. Mou,[5,*] and G. Pupillo[5]

[1]*Istituto Nazionale di Fisica Nucleare Sezione di Padova, via F. Marzolo, 8, I-35131 Padova, Italy*
[2]*Università di Pavia, Dipartimento di Fisica, via A. Bassi 6, I-27100 Pavia, Italy*
[3]*Istituto Nazionale di Fisica Nucleare Sezione di Pavia, via A. Bassi 6, I-27100 Pavia, Italy*
[4]*Università di Padova, Dipartimento di Fisica e Astronomia, via F. Marzolo, 8, I-35131 Padova, Italy*
[5]*Istituto Nazionale di Fisica Nucleare Laboratori Nazionali di Legnaro, Viale dell'Università, Legnaro, I-35020 Padova, Italy*
[6]*Subatech, Centre National de la Recherche Scientifique/IN2P3, IMT Atlantique, Université de Nantes, CS 20722, 44307 Nantes Cedex, France*
[7]*GIP ARRONAX, Rue Arronax 1, 44800 Saint-Herblain, France*

(Received 2 August 2021; accepted 24 September 2021; published 25 October 2021)

New data for the $^{\text{nat}}$V(p,x) reactions have been measured in the range 26–70 MeV, with production of the nuclides ^{47}Sc, ^{43}Sc, ^{44m}Sc, ^{44g}Sc, ^{46}Sc, ^{48}Sc, ^{42}K, ^{43}K, ^{48}V, ^{48}Cr, ^{49}Cr, and ^{51}Cr. The focus is on the production of ^{47}Sc, a β^- emitter suitable for innovative radiotheranostic applications in nuclear medicine. The measured cross sections for this radionuclide and its contaminants are compared with the theoretical excitation functions calculated with the TALYS code. In view of novel radiopharmaceutical applications, it is essential to accurately describe these cross sections for the evaluation of yields, purities, and dose releases. Hence, we optimize the level-density parameters of the microscopic models in the TALYS code to obtain the best possible descriptions of the new data. We consider different irradiation conditions to estimate the production yields from the cross sections determined in this paper.

DOI: 10.1103/PhysRevC.104.044619

I. INTRODUCTION

The theranostic radionuclide ^{47}Sc has gained the attention of the scientific community for its favorable decay characteristics ($T_{1/2}$=3.35 d, E_{β^-}=162 keV, E_γ=159 keV, I = 68.4%) [1] that make it one of the most attractive radionuclides for nuclear medicine applications [2]. In addition to its long half-life, suitable to follow the slow biodistribution of large molecules such as monoclonal antibodies, ^{47}Sc can be used for Single Photon Emission Computed Tomography imaging, thanks to its γ emission, and to treat small-size tumors, thanks to its high intensity low-range β^- radiation. The stable coordination of the Sc element with the chelating agent DOdecane Tetraacetic Acid paves the way to new ^{47}Sc radiopharmaceuticals, while the possibility to pair ^{47}Sc with its positron-emitter counterparts, ^{43}Sc and ^{44}Sc, permits one also to perform low dose Positron Emission Tomography studies before, during, and after therapy [3–5]. Despite some promising preclinical results, the use of ^{47}Sc-labeled radiopharmaceuticals in nuclear medicine is curtailed by the lack of ^{47}Sc availability in sufficiently high yield and medically acceptable purity [6]. For this reason, all possible ^{47}Sc product ion routes are investigated worldwide, considering both accelerators (cyclotrons and LINear ACcelerator) and nuclear reactors. The PASTA project (acronym for Production with Accelerator of Sc-47 for Theranostic Applications) aimed at measuring the most promising nuclear reactions to produce ^{47}Sc considering proton beams [7,8]. The project was developed in the framework of the LAboratory of RAdionuclides for MEDicine (LARAMED) program at the Istituto Nazionale di Fisica Nucleare (INFN) Legnaro National Laboratories (LNL), where a 70-MeV proton cyclotron was installed and the infrastructure for nuclear cross-section measurements and small-scale production of medical radionuclides for preclinical applications is under completion [9].

The fundamental role of nuclear physics in the production of radionuclides for medical applications is highlighted by several authors [3,6,10,11]. One of the major goals is to minimize the coproduction of contaminant isotopes during the irradiation since they cannot be separated with a radiochemical process. In the case of ^{47}Sc, the main contaminant is ^{46}Sc due to its long half-life (83.79 d) but the contribution to the final dose imparted to the patient has to be carefully analyzed considering the specificity of each radiopharmaceutical and all the scandium radionuclides coproduced [12] (see Table I for the main decay properties of the most relevant radionuclides discussed in this paper). In this context nuclear reaction models are of great aid to describe the cross sections, particularly for radionuclides or contaminants that are difficult

*liliana.mou@lnl.infn.it

to measure. For example, in the case of ^{47}Sc production, attention has to be paid to the coproduction of ^{45}Sc (stable) and ^{49}Sc, which emits low-intensity γ lines. Both nuclides could hardly be observed, but nevertheless they require an estimation since they affect the final isotopic purity and specific activity of the Sc-labeled radiopharmaceutical.

This paper is a compendium of the nuclear cross sections measured in the PASTA project by using proton beams and $^{\text{nat}}$V targets, namely, ^{47}Sc and Sc isotopes (^{43}Sc, ^{44m}Sc, ^{44g}Sc, ^{46}Sc, ^{48}Sc), ^{42}K, ^{43}K, ^{48}V, ^{48}Cr, ^{49}Cr, and ^{51}Cr. The experimental values regarding the production of these 12 radionuclides are compared with the literature. In particular, the case of ^{47}Sc has been studied since 1956 by Heininger [13], whose data cover the 60–240-MeV energy range. However, those results show the maximum experimentally observed deviation from the average literature and large uncertainties [14]. The values of the $^{\text{nat}}$V$(p,x)^{47}$Sc cross section obtained by Hontzeas and Yaffe in 1963 are very scattered and seem to not properly reproduce the trend of the reaction [15]; the peak, measured at 42 MeV, is overestimated and the more recent measurements agree on the evaporation peak at lower energies ($E_p < 40$ MeV). The group of Michel *et al.* measured the proton-induced reactions on $^{\text{nat}}$V targets in two experimental campaigns: the first, covering the 18.5–45-MeV range, was published in 1979 [16]; the second, covering the 50–200-MeV range, was published in 1985 [17]. The ^{47}Sc production cross section from these measurements is also in agreement with the data at low energies ($E < 30$ MeV) by Levkovski [18]. The more recent data, provided by Ditrói *et al.* in 2016, cover the 36–64-MeV energy window and were compared with results obtained by using EMPIRE and TALYS nuclear codes [19]. Similarly, the experimental values obtained within the PASTA project for the 26.5–70-MeV energy range are here compared with results obtained by using state-of-art nuclear models that will be discussed further on. The results will allow us to accurately estimate the production yields of ^{47}Sc and contaminants and to design an irradiation experiment for the production of ^{47}Sc with the highest isotopic and radionuclidic purities. A preliminary assessment of the optimal conditions was presented in Ref. [12] in which the energy interval 19–30 MeV was identified as the most promising by performing a parametric extrapolation at low energy of the available data: in this analysis we follow a different approach by considering a microscopic theoretical model and, by introducing the tuning of the level densities, we get an excellent reproduction of the data in the region (mass and energy) of interest. Thus, without any parametric-fit extrapolation of data at low energies, we obtain an optimized theoretical prediction of the yields, as well as of the contamination by stable isotopes, such as ^{45}Sc, which typically are not measurable by γ spectroscopy. The advantage is that a complete theoretical model has built in the accurate constraints (centrifugal and Coulomb repulsion, mass-threshold conditions, etc.) that are needed for a correct threshold behavior, while a simple fit extrapolation may be not so accurate.

Nuclear reaction codes incorporate a statistical evaporation module, generally based upon the Hauser-Feshbach theory [20]. Amongst the various aspects that enter in that formalism, a crucial role is played by the nuclear levels density (NLD), characterizing the excitation structure of the compound nuclei. Up to the last century, the description of NLD was based mainly upon phenomenological models that could lead to analytical forms quite flexible but depending largely on the adjustment of parameters to the available data. Many phenomenological NLD models have been developed along these lines, starting from the basic Fermi-gas model, to the composite Gilbert-Cameron model [21], or to the generalized-superfluid model [22].

It was only starting from the years 2000 that the microscopic descriptions became sufficiently accurate in the global NLD description, for an extremely large set of nuclides (about 8000/8500), to compete with the phenomenological models for practical applications. One of the first works was developed in Ref. [23], where effective Skyrme-type nucleon-nucleon interactions have been employed in the context of mean-field theories. The method used the Hartree-Fock plus Bardeen-Cooper-Schrieffer model (HF-BCS) to describe the many-body structure and to incorporate the pairing force. NLD was then calculated using a microscopic statistical method, as described also in Ref. [24].

Further advancements in microscopic NLD calculations were achieved in Refs. [25,26], by resorting to a more consistent (axially symmetric) Hartree-Fock-Bogoliubov (HFB) scheme with Skyrme interaction, with the NLD constructed using a shell-model combinatorial approach [27]. This lead to quite a few improvements, such as the determination of the parity dependence of the NLD, together with the inclusion of the collective aspects of both rotational and vibrational character in the theoretical description.

More recently, a new study has been completed [28] with improvements in the microscopic description of the collective effects, both vibrational and rotational, based on the use of a new Gogny-type nucleon-nucleon effective interaction in the HFB approach. Also, the introduction of a temperature-dependent generalization allowed one to take into account the evolution of the nuclear deformation with increasing excitation energy, an important aspect that has been disregarded in previous treatments.

Other important aspects of the theoretical description of nuclear reactions are the optical potential model used to describe the interaction and the preequilibrium model. TALYS provides state-of-art implementations for both and we have made calculations with all the available options. We have obtained excellent results with the Jeukenne-Lejeune-Mahaux (JLM) microscopic model for the optical potential, as explained in the following, and with the exciton model with numerical transition rates (default option) for preequilibrium. In all the calculations, the optical potential and preequilibrium models are used "as provided," while for the NLD we have obtained a significant improvement with the scaling procedure described in Sec. III B.

This nuclear reaction study is devoted to a specific practical application of nuclear medicine: the evaluation of the production route of the theranostic ^{47}Sc radionuclide, along with its main contaminants, using the cyclotron-based $^{\text{nat}}$V(p,x) channel. This application-oriented problem demands a model description of cross sections as close as possible to the experimental data, since many quantities (yields, radionuclidic

purities, etc.) are needed with high accuracy for the multidisciplinary evaluation of the production route. Indeed, a precise determination of the relevant quantities is important for the prediction of the amount of radio-pharmaceutical compound that can be produced in view of preclinical and clinical trials, for the evaluation of the dosimetric impact to the patient's organs, and for the appropriate radiochemistry separation techniques.

These practical aspects imply that a good reproduction of the relevant cross sections is much more important than the overall theoretical consistency of models. For this reason we have adjusted the NLD parameters for an optimal reproduction of the cross sections, even if it increases the discrepancy between observed and calculated nuclear-level cumulatives.

This paper presents the final and complete data set obtained by the PASTA experiment. In Sec. II, we illustrate the experimental techniques and procedures employed for the acquisition of the new data. However, for details of the apparatus and methods, we refer also to previous publications [7,29] where partial and preliminary data of the experiment have been published. In Sec. III, we illustrate the main considerations upon the models implied by the nuclear reaction code TALYS, and how we have used the NLD parameters to optimize the reproduction of the measured cross sections. The experimental/theoretical results are presented in Sec. IV, and in Sec. V we discuss their implications, including an evaluation of ^{47}Sc yield obtainable with a standard irradiation-condition setup. Concluding remarks are given in Sec. VI.

II. EXPERIMENTAL SETUP AND MEASUREMENTS

Since the beam line devoted to cross-section measurements for medical radionuclides production is not ready yet at INFN-LNL, the experiments of the PASTA project were performed at the ARRONAX facility [30]. Six irradiation runs were carried out using the low current (100 nA) proton beam with tunable energy (34–70 MeV), the target holder and collimator described in a previous work [29]. Stacked-foils targets, composed by a set of thin metallic ^{nat}V foils (purity $> 99.8\%$, thickness=20 μm) interchanged with monitor foils and ^{nat}Al energy degraders, were used in the experiments [7]. The ^{nat}Ni$(p,x)^{57}$Ni and the ^{27}Al$(p,x)^{24}$Na cross sections, recommended by the International Atomic Energy Agency (IAEA) [31], were considered as monitor reactions, respectively, for energies lower and higher than 40 MeV. ^{nat}Ni (purity $> 99.95\%$, thickness=10 μm) or ^{nat}Al (purity $> 99.0\%$, thickness=10 μm) foils were thus added in the stacked structure after each ^{nat}V target foil (see Fig. 1). The target was placed under normal atmosphere downstream of the

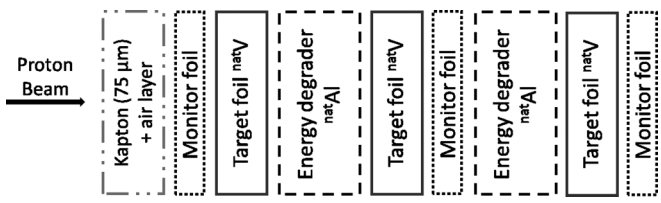

FIG. 1. Stacked-foils structure.

end of the beam line, kept under vacuum, and closed with a 75-μm-thick Kapton foil. The distance from the target holder to the Kapton foil, ranging from 10 to 15 cm, was accurately measured for each run. The proton beam energy entering each layer of the stacked-foils target was calculated using the SRIM code [32]. In order to calculate the energy losses in the Kapton foil, in the air, and across each target foil, the input parameters were the proton beam energy extracted from the cyclotron and each layer's thickness. At the end, each foil corresponds to one energy value, calculated as the mean energy of the input and output energies in the specific layer. The uncertainty of the proton beam energy was obtained considering the uncertainty of the beam energy extracted from the cyclotron (about 500 keV) and by calculating with the SRIM code the energy straggling through each layer of the stacked target.

All samples were measured with the same high-purity germanium detector (model Canberra GC1020, energy resolution full width at half maximum 1.0 keV at 122 keV, relative efficiency 10%), previously calibrated with a ^{152}Eu pointlike solid source. The sample-detector distance was fixed at 19 cm to keep the dead time during measurements below 10%. At least five acquisitions were carried out for each sample, in order to better follow the decay of the radionuclides of interest. The first measurement of each ^{nat}V foil, typically 15 min long, started about 2 h after the end of bombardment (EOB); the following acquisitions, usually 3 h long, were performed once per day starting from the day after the EOB (up to 5 days). An additional acquisition of each ^{nat}V foil was also carried out about 2 months after the EOB, to further measure the activity of the long-lived ^{46}Sc. Table I reports the decay characteristics of all radionuclides of interest, including the reference isotopes produced in the monitor foils, as extracted from the NuDat 2.8 database [1].

Data analysis, including uncertainty calculations, was performed following the procedure described in Ref. [33]. For the case of ^{44g}Sc, the activity was obtained by using the formulation presented in Ref. [33], that takes into account the ^{44m}Sc decay correction and the 1157-keV γ-line interference as shown in Table I. The final cross-section value related to each target foil was calculated as the weighted average of all single values associated to each counting; the uncertainty of the monitor cross section was added at the end of this calculation.

III. THEORETICAL CALCULATIONS

The theoretical analysis of cross sections for the production of medical radionuclides is important, since a good predictive capability is essential to efficiently guide the experimental activities. Conversely, new measurements are the key ingredient to validate the theoretical models and to optimize the models' free parameters. The topic has been thoroughly explored in the past and an exhaustive literature exists on the theory of nuclear reactions, ranging from phenomenological models that provide analytical expressions of important observables to modern microscopic approaches that aim for a more accurate description of the reaction mechanisms.

Modern nuclear reaction codes are today the best tools to perform theoretical calculations in this field: in this paper

TABLE I. Main decay characteristics of the 12 radionuclides of interest and of the two reference isotopes ^{57}Ni and ^{24}Na [1].

		γ emission		β emission			
Radionuclide	$\tau_{1/2}$	Energy (keV)	Intensity (%)	Mean β^+ energy (keV)	Total β^+ intensity (%)	Mean β^- energy (keV)	Total β^- intensity (%)
^{47}Sc	3.3492 d	159.381	68.3			162.0	100.0
^{43}Sc	3.891 h	372.9	22.5	476	88.1		
^{44m}Sc	58.61 h	271.241	86.74				
		1157.002	1.2				
^{44g}Sc	3.97 h	1157.02	99.9	632.0	94.27		
^{46}Sc	83.79 d	1120.545	99.9870			111.8	100.0000
		889.277	99.9840				
^{48}Sc	43.67 h	1312.120	100.1			220.4	100.0
		983.526	100.1				
		1037.522	97.6				
^{42}K	12.355 h	1524.6	18.08			1430.5	100.00
^{43}K	22.3 h	372.760	86.80			317	100.0
		617.490	79.2				
^{48}V	15.9735 d	983.525	99.98	290	49.9		
		1312.106	98.2				
		944.130	7.870				
^{48}Cr	21.56 h	308.24	100	96	1.6		
^{49}Cr	42.3 min	152.928	30.3	640	93		
^{51}Cr	27.704 d	320.0824	9.910				
^{57}Ni	35.60 h	1377.63	81.7	354	43.6		
		127.164	16.7				
^{24}Na	14.997 h	1368.626	99.9936			554.6	99.995

we have used the TALYS simulation package [34], which is actively developed and maintained. The aim of the authors is to provide a complete and high quality set of models [35] for the different reaction mechanisms that are relevant in the energy range of medical interest, namely, nuclear scattering, compound nucleus formation, and preequilibrium emission.

Recently, a great effort was made to implement different microscopic models, both for the optical potential and for the nuclear level densities. For the optical potential model, we have selected the so-called JLM semimicroscopic nucleon-nucleus spherical optical model potential as described in Ref. [36]. This model relies on the folding of a nucleon-nucleon effective interaction in nuclear matter. It is based upon the Brückner-Hartree-Fock theory to describe the mass operator in infinite nuclear matter, and then applied to finite nuclei via the improved local density approximation. To take into account the preequilibrium emission we have used the default option, which is based on the exciton model with transition rates evaluated numerically. Regarding nuclear level density, we focus in particular on the microscopic approach denoted as the Hartree-Fock model (HFM), which includes both HF-BCS and HFB descriptions, able to provide detailed information about nuclear energy levels as well as masses, spin, parity, and level density. The last parameter has been studied starting from the seminal work of Bethe [37] in the context of the compound nucleus theory and in many other phenomenological approaches, but from the physical point of view the microscopic approach provides a modern and flexible description of the level densities. Indicating with $N(E)$ the cumulative number of levels with energy smaller than E, the nuclear level density is defined as [38]

$$\rho(E) = \frac{dN(E)}{dE}. \tag{1}$$

This quantity can be inferred experimentally from different sources, such as spectroscopic studies, neutron resonances, evaporation spectra, and Ericson fluctuations studies [39]. Level density has been calculated in the HFM frameworks and the comparison is usually done by inspecting the cumulative distributions $N(E)$ [40].

A. Microscopic models in the TALYS code

Amongst the various options for the choice of the optical model in TALYS, the JLM microscopic optical model, derived according to the work reported in Refs. [41,42], was then adjusted phenomenologically [36] to improve the agreement of calculated finite-nuclei cross sections with a large set of experimental data.

Moreover TALYS provides a variety of HFM based microscopic frameworks for the level density with three different tabulated options: *ldmodel 4* [microscopic level densities (Skyrme force) from Goriely's tables [23]], *ldmodel 5* [microscopic level densities (Skyrme force) from Hilaire's combinatorial tables [26]], and *ldmodel 6* [microscopic level densities (temperature dependent HFB, Gogny force) from Hilaire's combinatorial tables [28]].

The three models are based on the HFM approach and represent somehow the time evolution of the TALYS code with respect to the microscopic level density models, as suggested by the referenced papers. None of them is perfect, but they complement each other being able to describe different aspects of reaction mechanisms, possibly on the entire nuclide chart. Each option provides different tabulated level densities, but the code allows one to overrule them to improve the agreement with data within a restricted Z and A range. In this paper we have found good results with the option *ldmodel 4* and with an optimized set of parameters that were applied to the calculations by a scaling procedure. The preequilibrium model is fixed in all calculations with the option *preeqmode 2*, except for the ^{51}Cr cross section where we have sought for an improvement with a more recent addition as discussed in the following.

There is a relevant limitation in the reaction codes that are currently used for nuclear application analyses, including the ones discussed in this paper, concerning the isospin dependence. Indeed, quite a few years ago, it has been pointed out in Ref. [43] that the Hauser-Feshbach formalism should include an isospin dependence since this affects significantly the first proton-emission branching in proton-induced reaction on nonzero isospin targets. Inclusion of isospin-coupling effects [44] also has an impact on nuclear-level densities, which could require the consideration of additional isospin information, more detailed than those actually in use in current nuclear reaction codes. It is clear that the absence of such isospin dependence in the codes used in the present paper might contribute to the need of a specific optimization of the nuclear level densities, to improve the reproduction of the cross sections.

B. Nuclear level density scaling procedure

The approach used in TALYS offers a certain level of flexibility since, in the HFM description, the level densities are tabulated at different excitation energies for both parities and different values of spins: the values in these tables can be rescaled by simple multiplication to fit experimental data. This technique has been successfully adopted in Ref. [45] to find a global best fit on the entire nuclide chart.

In general the original HFM microscopic level densities have not been adjusted to experimental data and the tabulated values can be rescaled by using two parameters (c and p) according to the transformation

$$\rho(E, J, \pi) = \exp(c\sqrt{E-p})\rho_{\mathrm{HFM}}(E-p, J, \pi) \qquad (2)$$

The parameter p is called "pairing shift" in TALYS and allows one to obtain the level density from the table at a different energy, and could also represent an energy shift caused by pairing or even shell effects. Parameter c acts to the level density in a similar way to that of the parameter a of phenomenological models and provides an overall normalization of the level density. Adjusting p and c together provides flexibility in fitting at both low and high energies, and this implies that both low-energy discrete levels and average experimental resonance separations can be described within the same procedure. This procedure allows one to modify the original HFM level density and to obtain different "customized" tables, as shown in the TALYS manual and on the Reference Input Parameter Library (RIPL) library [40].

TABLE II. Optimized c and p parameters used in this paper.

Isotope	c	p
^{42}K	1.27443	
^{43}K	1.09559	0.140468
^{44}Sc	1.97876	1.11855
^{46}Sc	0.339592	−1.17731
^{48}Sc		0.449064
^{48}V		−0.25841
^{48}Cr	0.234421	

1. Grid search and optimization procedure

The first step is a grid search on the c and p parameters in the allowed range $[-10, 10]$ [46], but we have restricted our search in a narrower interval $[-2, 4]$ as suggested by Fig. 39 in Ref. [40]. The grid search is multidimensional, since it concerns the c and p parameters of all the nuclides involved. A preliminary solution is found by a first qualitative agreement between theory and measurements, obtained by visual inspection of the cross sections for which new data are available. With this trial and error approach, we define the initial values of the c and p parameters for the next step, characterized by the optimization procedure.

The second step is to refine the solution by evaluating a global chi-square of all the involved cross sections: a MINUIT-based chi-square minimization procedure [47] has been implemented by using the c and p values as free parameters, with initial values identified by the previously described grid search. The minimization algorithm used is the MINUIT recommended one, which is based on the combination of gradient and simplex optimization. The level density distributions and cumulatives associated to the theoretical cross sections that correspond to the minimum chi-square are analyzed and compared with the default HFB and the TALYS proposed ones.

The goal of this paper is to achieve the most accurate parametrization of the selected TALYS microscopic model for the cross sections of interest. Following these steps we have found an optimized set of values for the c and p parameters to fit our experimental cross sections and we have analyzed the corresponding cumulative distributions of levels. We report these optimized values, found for the subset of analyzed isotopes, in Table II. For a few of the nuclides reported in the table, it was necessary to vary only one parameter (c or p), maintaining the other unchanged with respect to the value defined by the Goriely tables adopted in *ldmodel 4*. The solution that we have found in Table II is not necessarily unique: we cannot exclude that another set of parameters (related for example to a different optical potential, preequilibrium, or nuclear level density model) could reproduce the data with a similar accuracy. This would still be in the spirit of this paper, i.e., to improve the theoretical description of the cross sections of medical radioisotopes and contaminants for radiopharmaceutical applications.

TABLE III. Experimental values of the 12 cross sections measured in this paper for the nuclear reactions $^{nat}V(p,x)$.

Energy	^{47}Sc	^{43}Sc	^{44g}Sc	^{44m}Sc	^{46}Sc	^{48}Sc	^{42}K	^{43}K	^{48}V	^{48}Cr	^{49}Cr	^{51}Cr
70.0 ± 0.6	8.0 ± 0.4	0.4 ± 0.1	8.7 ± 0.6	8.0 ± 0.4	16.4 ± 0.9	2.3 ± 0.2	2.0 ± 0.1	0.27 ± 0.02	72.4 ± 6.7	1.1 ± 0.1	6.2 ± 1.0	10.9 ± 1.0
67.8 ± 0.7	7.7 ± 0.5	0.3 ± 0.1	7.3 ± 0.6	7.0 ± 0.4	16.7 ± 1.0	2.4 ± 0.2	2.0 ± 0.1	0.30 ± 0.02	79.0 ± 7.2	1.3 ± 0.1	6.8 ± 1.1	11.7 ± 1.1
65.5 ± 0.8	6.8 ± 0.4	0.1 ± 0.1	5.7 ± 0.5	5.2 ± 0.3	16.7 ± 1.0	2.3 ± 0.2	1.9 ± 0.1	0.32 ± 0.02	80.9 ± 11.2	1.4 ± 0.1	7.2 ± 0.8	11.8 ± 0.9
60.7 ± 0.6	5.1 ± 0.3	0.3 ± 0.3	2.1 ± 0.2	1.9 ± 0.1	18.6 ± 1.2	1.9 ± 0.1	1.3 ± 0.1	0.39 ± 0.03	91.8 ± 7.6	1.7 ± 0.1	9.1 ± 1.0	16.5 ± 1.2
58.3 ± 0.7	5.0 ± 0.4	0.1 ± 0.1	1.2 ± 0.1	1.1 ± 0.1	21.6 ± 1.8	1.8 ± 0.1	0.9 ± 0.1	0.43 ± 0.04	103.3 ± 10.6	1.9 ± 0.2	10.6 ± 1.3	18.3 ± 1.6
55.7 ± 0.8	4.4 ± 0.4	0.05 ± 0.03	0.6 ± 0.1	0.47 ± 0.04	23.0 ± 1.9	1.4 ± 0.1	0.48 ± 0.05	0.42 ± 0.04	100.9 ± 9.8	1.9 ± 0.2	11.2 ± 1.2	18.4 ± 1.7
53.6 ± 0.6	4.1 ± 0.3	0.07 ± 0.04	0.35 ± 0.03	0.25 ± 0.02	25.1 ± 2.0	1.0 ± 0.1	0.26 ± 0.03	0.41 ± 0.03	100.8 ± 9.8	1.8 ± 0.1	12.1 ± 1.5	16.8 ± 1.4
51.0 ± 0.7	4.1 ± 0.3	0.1 ± 0.1	0.19 ± 0.04	0.13 ± 0.01	27.8 ± 2.3	0.7 ± 0.1	0.07 ± 0.01	0.32 ± 0.03	91.1 ± 9.3	1.5 ± 0.1	14.2 ± 1.7	17.3 ± 1.6
48.1 ± 0.8	4.6 ± 0.3	0.4 ± 0.2	0.17 ± 0.05	0.05 ± 0.01	30.8 ± 2.4	0.37 ± 0.03		0.20 ± 0.02	74.5 ± 7.3	1.0 ± 0.1	18.3 ± 2.6	19.7 ± 1.8
39.5 ± 0.6	8.3 ± 0.5				18.6 ± 1.1				8.3 ± 0.8		28.9 ± 2.8	25.7 ± 1.6
33.3 ± 0.6	10.9 ± 0.6				2.6 ± 0.2				2.4 ± 0.2		25.3 ± 2.6	32.3 ± 1.9
31.2 ± 0.7	9.0 ± 0.5				0.6 ± 0.1				1.2 ± 0.1		17.2 ± 1.7	34.1 ± 2.0
29.2 ± 0.8	7.4 ± 0.5								0.40 ± 0.02		8.3 ± 0.9	33.7 ± 2.2
26.5 ± 0.8	4.3 ± 0.2								0.15 ± 0.02		0.7 ± 0.1	46.2 ± 2.9

IV. RESULTS

This paper provides new nuclear reaction data for cross sections induced by protons on ^{nat}V targets, within the energy range 26–70 MeV. Table III and Figs. 2–14 report the experimental cross-section values obtained for the $^{nat}V(p,x)^{47}$Sc, ^{43}Sc, ^{44g}Sc, ^{44m}Sc, ^{46}Sc, ^{48}Sc, ^{43}K, ^{42}K, ^{48}V, ^{48}Cr, ^{49}Cr, and ^{51}Cr reactions. The maximum value for the beam energy uncertainty, including the energy straggling, was 0.8 MeV. The $^{nat}V(p,x)^{47}$Sc, ^{46}Sc cross-section values were already presented in a work dedicated to ^{47}Sc production by using ^{nat}V targets [7]. Also the case of ^{43}Sc and ^{43}K radionuclides was described in a specific article, since an evident discrepancy with previous results was found [29]. The new data are compared with the literature, the default TALYS results (corresponding to the following options: Koning-Delaroche phenomenological optical potential, exciton model preequilibrium, and constant temperature Fermi-gas model level density), and the modified TALYS calculation discussed in Sec. III. The fit turned out remarkably close to the data, not only closer than the default calculation, but also closer than the other predefined models (*ldmodel 4,5,6*), and this has important consequences for the evaluation of the ^{47}Sc production route for applications in nuclear medicine.

V. DISCUSSION

A. On experimental data

A general good agreement among the new results obtained in this paper with the literature data has been found, except with the first data published in 1956 and 1963 [13,15], probably due to the use of old nuclear and monitor values in those analyses. The largest discrepancy with previous data was found for the ^{43}Sc case (Fig. 3), as described in the specific work that includes also ^{43}K production (Fig. 9) [29]. Since the $^{nat}V(p,x)^{47}$Sc and ^{46t}Sc cross sections measured within the PASTA project (Figs. 2 and 6) were already presented in Ref. [7], a detailed discussion is here referred to the production of ^{44}Sc, ^{44m}Sc, ^{48}Sc, ^{48}V, ^{48}Cr, ^{49}Cr, ^{51}Cr, and ^{42}K. As shown in Figs. 4 and 5, the cross sections regarding ^{44}Sc and ^{44m}Sc are in good agreement with previous data, especially with Ditrói *et al.* [19]. However, our results for ^{44}Sc at high energies ($E > 65$ MeV) are slightly higher than the trend indicated by those data up to 60 MeV. The value at 70 MeV obtained by Hontzeas and Yaffe [15] is lower than our result, and the same discrepancy can be found for the ^{44m}Sc case (Fig. 5). For the $^{nat}V(p,x)^{44m}$Sc cross section, the results obtained by Michel *et al.* in 1985 [17] confirm the trend that we have measured.

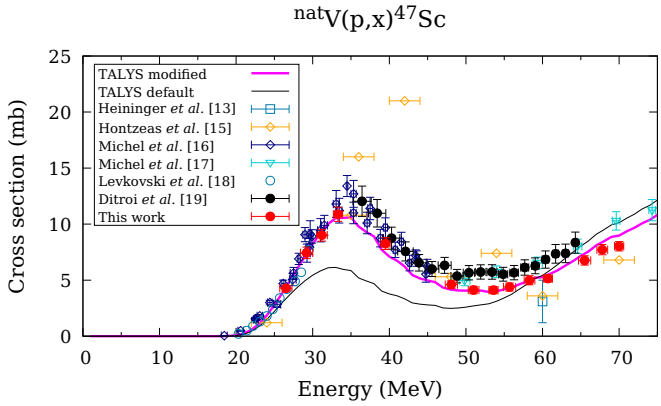

FIG. 2. ^{47}Sc cross section.

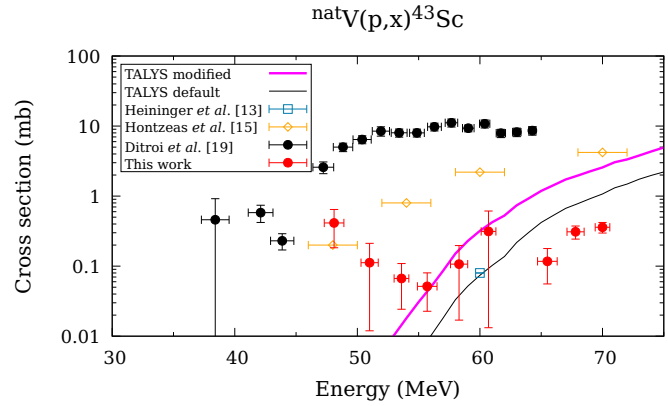

FIG. 3. ^{43}Sc cross section.

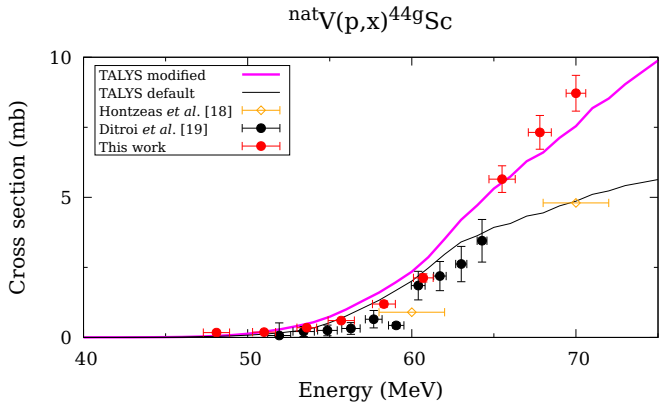

FIG. 4. ^{44g}Sc cross section.

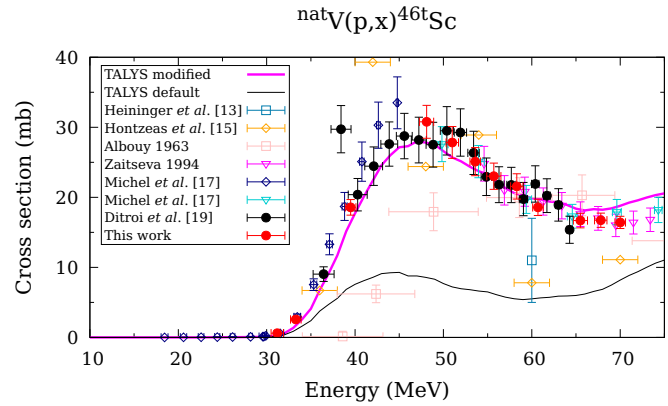

FIG. 6. ^{46}Sc cross section. The ^{46t}Sc notation indicates the cumulative cross section due to the formation of the metastable (half-life: 18.75 s) and ground state of ^{46}Sc.

In the data analysis of ^{48}Sc production, only the 1037.52-keV γ line was considered, since the 1312.12- and 983.526-keV lines are emitted also by ^{48}V (see Table I). Figure 7 reports the new data for the $^{\text{nat}}\text{V}(p,x)^{48}\text{Sc}$ cross section, in excellent agreement with the literature [17,19] except for data published in 1963 [15]. The $^{\text{nat}}\text{V}(p,x)^{48}\text{V}$ cross section, obtained considering the 944.13-keV γ line, is shown in Fig. 10: also in this case a very good agreement can be noted among the new and previous data in the entire energy range [16,17,19], also including the oldest values [13,15].

Figure 11 reports the cross section for ^{48}Cr production: in the entire energy range an excellent agreement can be seen among our results and the ones published in 2016 [19], that at low energy ($E < 45$ MeV) also matching with data by Michel *et al.* [16]. Instead, oldest values are quite scattered [13,15]. In the case of ^{49}Cr (Fig. 12) the maximum peak value that we obtained is lower than the one published by Michel *et al.* in 1979 [16], even if the peak energy seems to correspond. Concerning the Levkovski data [18], as already discussed in Ref. [7], they have been corrected by a factor of 0.77 in Figs. 2, 12, and 13 (indicated with a star in the legends). The eventual correction for the use of obsolete nuclear data (for the 153-keV γ line, they used 42-min half-life and 29.5% intensity instead of 42.3-min half-life and 30.3% intensity; see Table I) is too small to explain our peak value of about 40% lower.

The $^{\text{nat}}\text{V}(p,x)^{51}\text{Cr}$ cross section measured in this paper is in excellent agreement with the extensive literature (Fig. 14). Also for the $^{\text{nat}}\text{V}(p,x)^{42}\text{K}$ there is a very good agreement with previous data published by Ditrói *et al.* and Michel *et al.* [17,19]; the previous values at 60 MeV are much lower [13,15].

B. On theoretical models

The new calculations for ^{47}Sc and ^{46}Sc with the TALYS-modified code (shown in Figs. 2 and 6) greatly improve the agreement with the new measurements, particularly around the peak, where the level density models have an important role. The goodness of the data reproduction is essential in both cases.

In Figs. 3, 8, and 9, the new calculation provides a larger cross section than the default one, and for the two potassium productions, ^{42}K and ^{43}K, it reproduces the measured data very well. For ^{43}Sc, both calculations support the current measurements, however the trend of these new data exhibits an oscillatory behavior that cannot be reproduced by the models and that may be ascribed to statistical fluctuations originating from the low counts of the measurements [29].

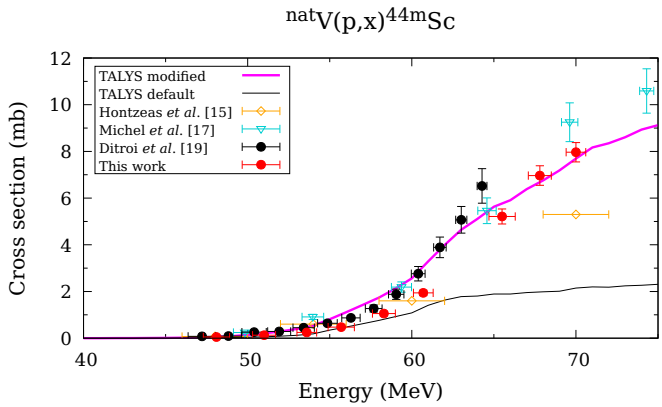

FIG. 5. ^{44m}Sc cross section.

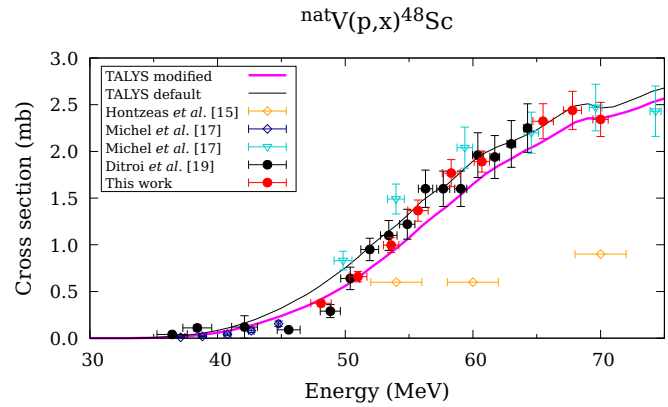

FIG. 7. ^{48}Sc cross section.

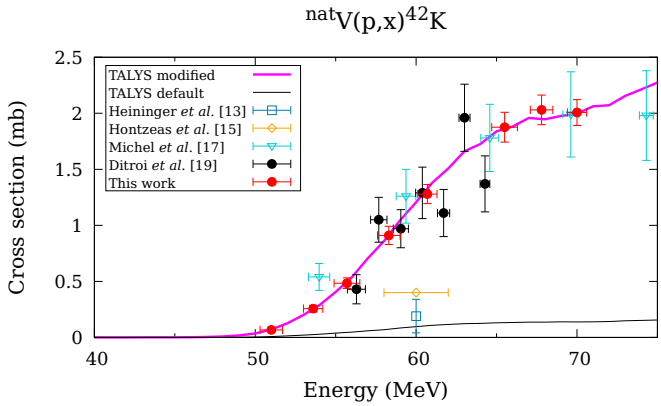

FIG. 8. ^{42}K cross section.

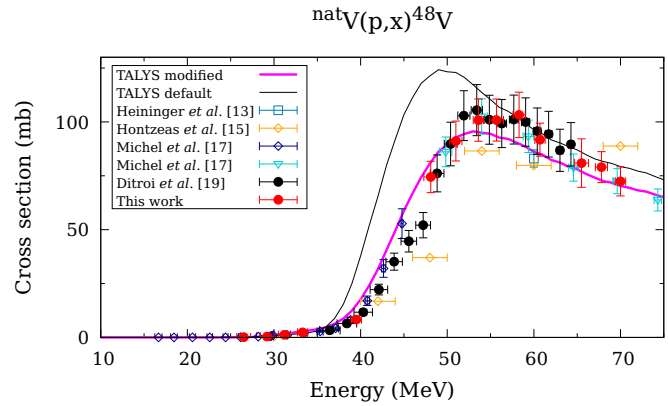

FIG. 10. ^{48}V cross section.

Additional scandium radionuclides with higher-energy thresholds are shown in Figs. 4, 5, and 7. In the case of ^{44g}Sc (ground) and ^{44m}Sc (metastable) the new calculation reproduces the data in the entire energy range while the default one underestimates the data in the higher-energy region. For ^{48}Sc, both calculations reproduce the measurements within the experimental uncertainties, but the TALYS modified result describes better the low-energy rise close to threshold and around 45 MeV.

In Figs. 10–12, the improvement of the modified TALYS calculation with respect to the default one is also very significant. All the cross sections calculated with the default option show a clear offset in the peak position, corrected in the new calculation. The changes triggered by the new calculation have been analyzed in detail: the correct reproduction is achieved by the combined effects generated by the optical potential (the JLM optical potential), and by the selected NLD model (*ldmodel 4*), further adjusted with the local optimization of the *c* and *p* parameters (modified). It is worth noting that the level density parameters have been fitted to the new data obtained with this paper, but, in Fig. 12, the resulting cross section better reproduces the peak value measured in Ref. [16].

Finally, in Fig. 13, we provide also the results for ^{51}Cr production. The new calculation improves the reproduction of data, particularly in the range 15–20 MeV. This is confirmed in the same region also if we compare the two calculations with the IAEA recommended data [48]. In the peak range and at lower energies, both calculations show slight discrepancies when compared with the IAEA recommended evaluation. For this reaction, it is interesting to consider the range at higher energy, where the new data have been collected and where the preequilibrium mechanisms play a more significant role. This region is analyzed in detail in Fig. 14, where it is evident that neither of the two calculations (TALYS default and modified) describes correctly the data. We have considered additional new calculations with different preequilibrium models in order to seek a better description in this specific channel. The recent TALYS-1.95 GDH version [49], in which the geometry dependent hybrid (GDH) model [50,51] was added, has been exploited: this model was previously implemented in other codes, such as ALICE [52], and has been included in the TALYS package by the authors [49]. The calculated excitation function with the GDH model better reproduces the experimental data and this supports the good performance of this newly added preequilibrium feature in the TALYS framework. Another reaction code, known to give good description at intermediate energy, is FLUKA [53,54]. In this code the production of residual nuclei is based on the PEANUT (PreEquilibrium Approach to NUclear Thermalisation) model, which couples a classical intranuclear cascade

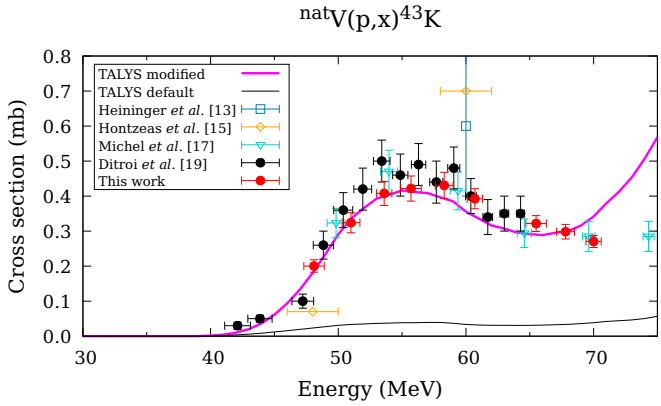

FIG. 9. ^{43}K cross section.

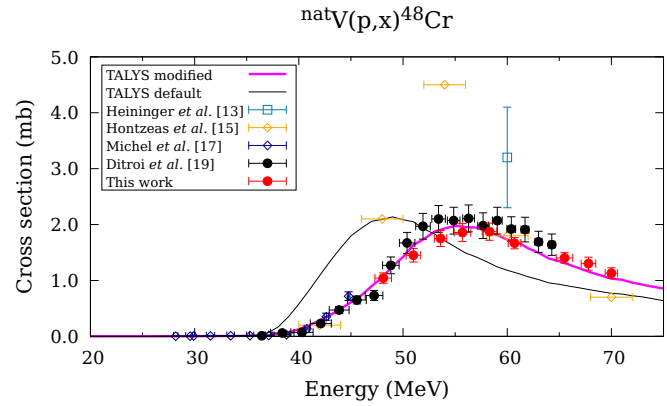

FIG. 11. ^{48}Cr cross section.

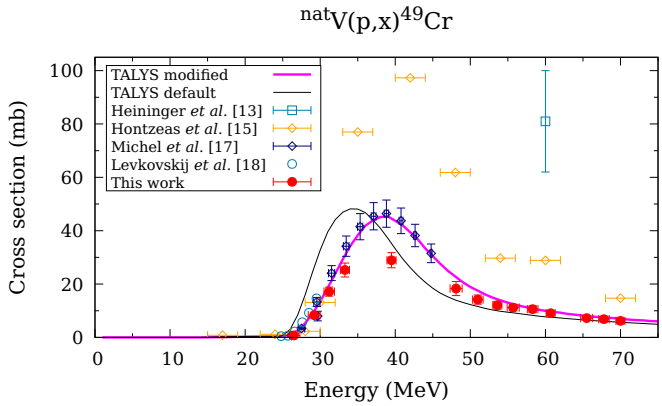

FIG. 12. ^{49}Cr cross section.

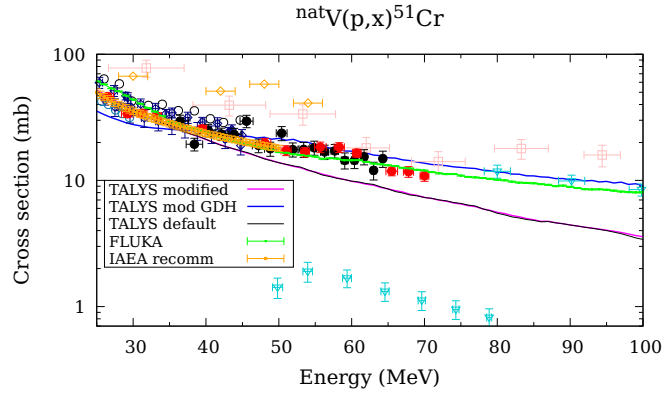

FIG. 14. ^{51}Cr cross section.

model, supplemented with quantum corrections, with a preequilibrium framework inspired by the GDH approach. In this framework the produced radionuclides emerge directly from the inelastic hadronic interaction models that are based on a microscopic description of the nucleon-nucleon interaction. This approach is not recommended for the calculation of cross sections at very-low energies, close to the reaction thresholds, but, generally, provides reliable results at higher energies. As shown in Fig. 14, FLUKA is able to reproduce the ^{51}Cr cross-section high-energy tail with an excellent agreement with the new experimental data.

The importance of the theoretical modeling strikingly emerges when one considers the production of stable nuclides, since their cross sections cannot be measured with standard γ-spectroscopy techniques. Such is the case for the ^{45}Sc isotope, shown in Fig. 15. The new cross section exhibits remarkable differences compared to the default one. Without data it is difficult to draw conclusive statements; however, the fact that it provides the correct results for the contiguous reactions (see Figs. 4–6) makes the new ^{45}Sc result certainly more credible than the TALYS-default result. A reliable theoretical estimate of stable contaminant production is crucial for the production of radio pharmaceuticals, since ^{45}Sc contamination can affect significantly the specific activity of produced ^{47}Sc, in the complete absence of relevant cross-section data.

The parameters for the level density found in the predefined TALYS models are introduced on a global scale, suitable for a broad set of nuclides. In our case we have found a minimal subset of the same parameters that allow one to accurately describe the measured channels, without aiming at a self-consistent global reaction model. In more detail, we redefined the single c parameter for ^{42}K and ^{48}Cr, the single p parameter for ^{48}Sc and ^{48}V, and both c and p for ^{43}K, ^{44}Sc, and ^{46}Sc. The corresponding values are given in Table II. This parametrization leads to a solution that optimizes the production of ^{47}Sc for theranostic applications in agreement with the measurements presented in this paper, and allows one to accurately calculate the yields and isotopic/radionuclidic purities for realistic irradiation conditions. Our modified nuclear level density is however different from the previous ones and it is important to assess the effect of the transformation given by Eq. (2) by comparing the theoretical cumulative level distribution with the experimental one deduced from RIPL. This comparison is presented in Fig. 16, where the cumulatives from the HF-BCS model are compared with Goriely's global analysis and with the fit obtained in this paper. We stress that the parametrizations given in Table II do not improve substantially the agreement between theoretical and

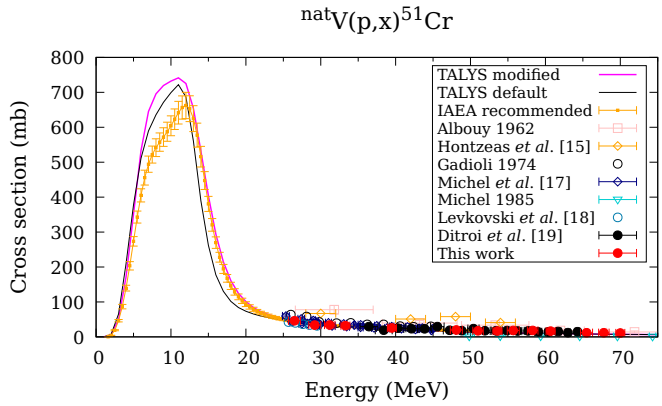

FIG. 13. ^{51}Cr cross section. The plot below 25 MeV only shows the IAEA recommended evaluation, which represents a guide for the copious number of data measured around the peak.

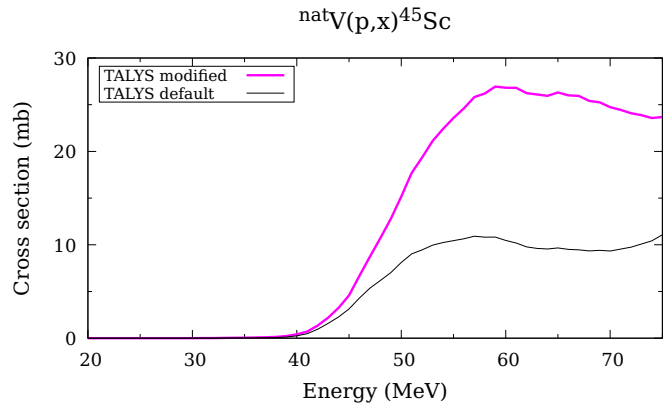

FIG. 15. ^{45}Sc cross section.

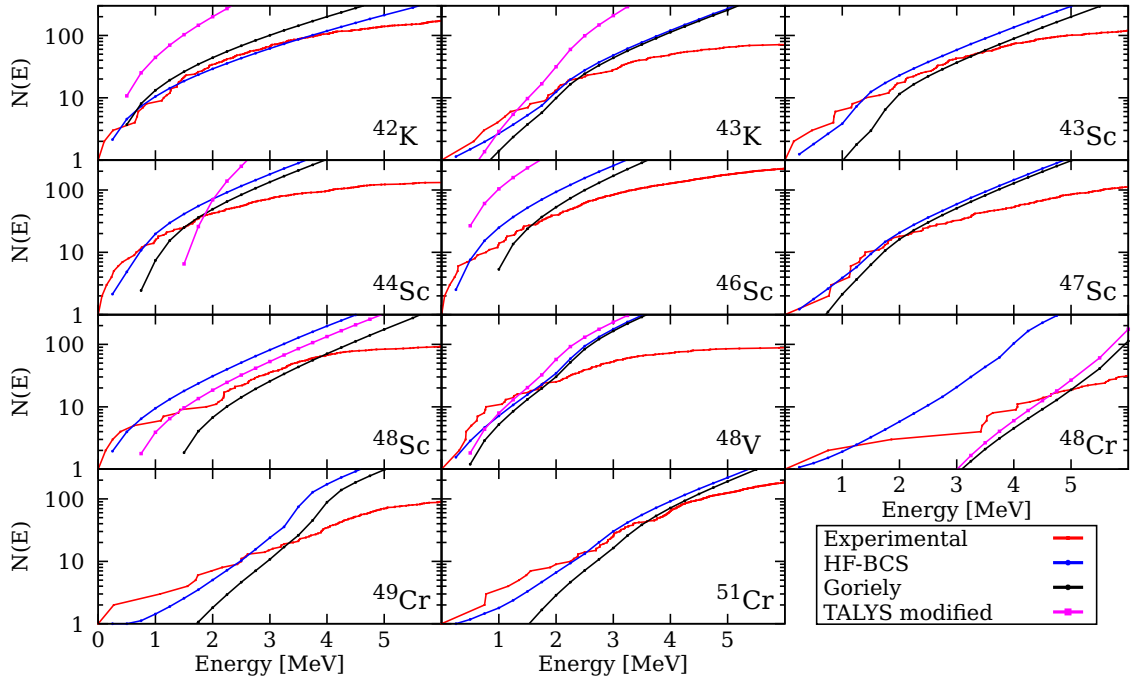

FIG. 16. Comparison of the observed cumulative levels with the theoretical models discussed in the text.

experimental cumulatives: that was not our scope. Our aim is to find the best description for the relevant cross sections in view of their importance in radiopharmaceutical applications, and for this reason we have derived the new parameters reported in Table II.

C. Thick target yield

We have calculated the ^{47}Sc production yield in the same irradiation conditions identified in Ref. [12]. The yield calculations are developed along the lines discussed in Ref. [20]. The energy range 19–30 MeV, corresponding to a 1.21-mm-thick target perpendicular to the proton beam, can be chosen to avoid ^{46}Sc coproduction. Considering an irradiation time of 24 and 80 h it is possible to achieve a sufficient amount of ^{47}Sc with the highest purity to start preclinical and clinical trials. The results are shown in Table IV, where we use the cross section obtained with TALYS default and with TALYS modified as discussed in this paper. To complete the comparison, we also add the values obtained with the low-energy extrapolation (polynomial fit) discussed in Ref. [12] as well as the results obtained with the online tool ISOTOPIA, developed at IAEA. We refer to Refs. [55,56] for a detailed description of the simulations provided by ISOTOPIA.

From Table IV we observe that, for the ^{47}Sc yield, TALYS default and ISOTOPIA give very similar results, while for ^{46}Sc ISOTOPIA gives estimates four times lower than TALYS default. Both calculations, however, seem to underestimate substantially the ^{47}Sc yield, and even more severely the yield of the ^{46}Sc contaminant, when compared with TALYS modified (this paper) or with the polynomial fit of Ref. [12]. This difference may be ascribed to the fact that both TALYS modified and the polynomial fit adhere more closely to the measurements. The differences between TALYS modified and the polynomial fit amount to a 21% increase for the latter, for both ^{47}Sc and ^{46}Sc yields. We have inspected the low-energy behavior of the cross sections in Figs. 17 and 18. For ^{47}Sc, TALYS modified reproduces the low-energy regime reported by the data in an optimal way, while in the case of ^{46}Sc the calculation slightly underestimates the data by Michel *et al.* [16]. The low-energy extrapolation of the polynomial fit appears somewhat critical and not completely under control, being built on data sets measured at quite higher energies. On the other hand, the TALYS modified solution is more reliable than the polynomial fit in the threshold region because it contains all the physical effects due to energy (mass threshold) and angular momentum (centrifugal barrier) conservation and to the Coulomb barrier:

TABLE IV. Theoretical thick target yield at EOB of ^{47}Sc and its main contaminant ^{46}Sc with the different models considered in the analysis for the irradiation profile discussed in the text.

Radionuclide	Irradiation time (h)	TALYS default (MBq/μA)	TALYS modified (MBq/μA)	Polynomial fit (MBq/μA)	ISOTOPIA (MBq/μA)
^{47}Sc	24	24.43	33.48	41.50	25.29
^{46}Sc	24	0.0049	0.0137	0.0149	0.0013
^{47}Sc	80	65.12	89.24	111.00	67.43
^{46}Sc	80	0.0164	0.0453	0.0492	0.0042

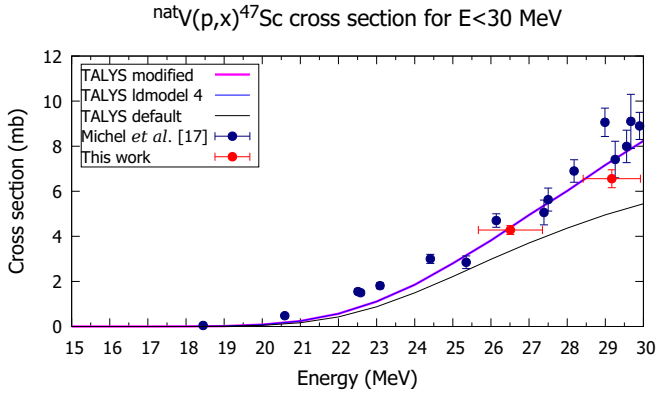

FIG. 17. Threshold of the $^{\text{nat}}\text{V}(p,x)^{47}\text{Sc}$ cross section.

all these constraints are absent in a low-energy extrapolation with a polynomial that, for this reason, might be inaccurate.

In Table V we compare the production (at EOB) of ^{45}Sc, ^{46}Sc, and ^{47}Sc in terms of number of produced nuclei. The impact of ^{45}Sc contamination appears negligible for both calculations.

VI. CONCLUSIONS

This paper reports new data for 12 proton-induced cross sections on a $^{\text{nat}}$V target that have been measured in the context of practical applications of novel radiopharmaceutical production. Along with the experimental measurements, we have studied the phenomenological cross-section modeling to obtain theoretical curves close to the data, as much as possible. The result has been obtained by using TALYS's microscopic models developed in the HF-BCS framework, and by performing a specific optimization of the parameters governing the nuclear level density. It is possible that the need of such optimization originates from significant contributions not yet included in the nuclear reaction codes, but already pointed out in the literature, such as the addition of isospin dependence in statistical processes. Concerning the preequilibrium models employed, we have selected in TALYS the (default) exciton model with numerically calculated transition rates. This option resulted adequate for the analysis of all

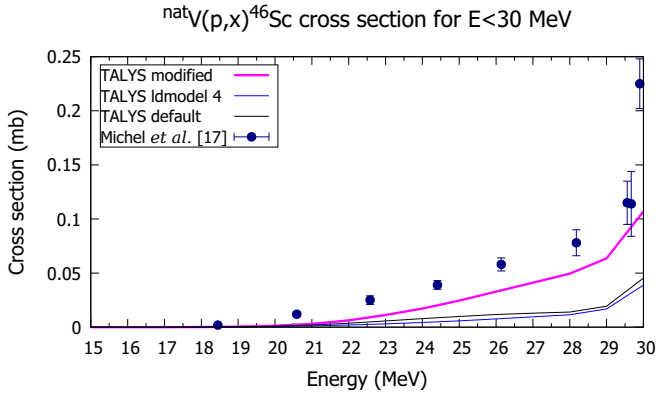

FIG. 18. Threshold of the $^{\text{nat}}\text{V}(p,x)^{46}\text{Sc}$ cross section.

TABLE V. Number of nuclei produced after a 24-h irradiation of the thick vanadium target. The two radioactive nuclides are compared with the stable isotope ^{45}Sc.

Radionuclide	Irradiation time (h)	TALYS default (no. of nuclei)	TALYS modified (no. of nuclei)
^{45}Sc	24	3.15×10^{9}	2.07×10^{9}
^{46}Sc	24	5.18×10^{10}	1.43×10^{11}
^{47}Sc	24	1.02×10^{13}	1.40×10^{13}

cross sections, with the exception of the high-energy tail of the ^{51}Cr one. We tested that the GDH preequilibrium model, that was recently added to the TALYS package, describes quite well the cross section in this higher-energy region, and is comparable with FLUKA results, a nuclear reaction package suited for modeling cross sections in the intermediate-energy region.

This paper supports the validity of the approach for nuclear medicine applications and provides an accurate estimation for the yields of ^{47}Sc and its main contaminants, leading to more reliable assessments of the production route and associated dosimetric analyses. In spite of some minor differences shown in Table IV, this paper confirms the proton-vanadium route in the 19–30-MeV range as a viable method for producing ^{47}Sc, with a low activity of ^{46}Sc and very minimal contamination of stable ^{45}Sc. It would be interesting, at this point, to confirm these findings with a dedicated thick target yield experiment with a thick vanadium target to be irradiated with protons in the suggested energy range. The produced ^{47}Sc quantities are sufficient for preclinical and clinical phase trials. To get higher activities, work must be done either on other production routes (either using neutrons or photoproduction) or on targetry to accommodate mA proton beams.

It is important to observe that the tuning of the theoretical level density parameters to obtain accurate cross sections is of general applicability for analyzing possible production routes also for other innovative radionuclides for medical applications.

ACKNOWLEDGMENTS

The authors thank Dr. Juan Esposito and Dr. Carlos Rossi Alvarez for private communications and enlightening scientific discussion, the LARAMED team, and the Accelerator for Research in Radiochemistry and Oncology in Nantes-Atlantique (ARRONAX) staff for support in the PASTA project. This work has been supported by Commissione Scientifica Nazionale 5 (CSN5) of Istituto Nazionale di Fisica Nucleare with a PASTA grant (Grant No. 2017/2018). This work has been partially supported by European Union Horizon 2020 project Research and Innovation action (RIA)-European Nuclear Science and Application Research 2 (ENSAR2) (Project No. 654 02); by grants from the French National Agency for Research called "Investissements d'Avenir", Equipex Arronax-Plus (ANR-11-EQPX-0004), Labex IRON (ANR-11-LABX-18-01), ISITE NExT (ANR-16-IDEX-0007) and INCa-DGOS-Inserm_12558.

[1] National Nuclear Data Center, NuDat 2.8 database, https://www.nndc.bnl.gov/, accessed March 2021.

[2] A. R. Jalilian *et al.*, IAEA activities on ^{67}Cu, ^{186}Re, ^{47}Sc Theranostic radionuclides and radiopharmaceuticals, Curr. Radiopharm. **14**, 306 (2021).

[3] *Therapeutic Radiopharmaceuticals Labelled with Copper-67, Rhenium-186 and Scandium-47*, TECDOC Series Vol. 1945 (International Atomic Energy Agency, Vienna, 2021).

[4] C. Müller, K. A. Domnanich, C. A. Umbricht, and N. P. van der Meulen, Scandium and terbium radionuclides for radiotheranostics: Current state of development towards clinical application, Br. J. Radiol. **91**, 20180074 (2018).

[5] C. S. Loveless, L. L. Radford, S. J. Ferran, S. L. Queern, M. R. Shepherd, and S. E. Lapi, Photonuclear production, chemistry, and in vitro evaluation of the theranostic radionuclide ^{47}Sc, EJNMMI Res. **9**, 1 (2019).

[6] S. M. Qaim, *Medical Radionuclide Production: Science and Technology* (De Gruyter, Berlin, Boston, 2020), p. 270.

[7] G. Pupillo, L. Mou, A. Boschi, S. Calzaferri, L. Canton, S. Cisternino, L. De Dominicis, A. Duatti, A. Fontana, F. Haddad *et al.*, Production of ^{47}Sc with natural vanadium targets: Results of the pasta project, J. Radiol. Nucl. Chem. **322**, 1711 (2019).

[8] G. Pupillo, A. Fontana, L. Canton, F. Haddad, and H. Skliarova, Preliminary results of the PASTA project, Il Nuovo Cimento C **42**, 139 (2019).

[9] J. Esposito, D. Bettoni, A. Boschi, M. Calderolla, S. Cisternino, G. Fiorentini, G. Keppel, P. Martini, M. Maggiore, L. Mou, M. Pasquali, L. Pranovi, G. Pupillo, C. Rossi Alvarez, L. Sarchiapone, G. Sciacca, H. Skliarova, P. Favaron, A. Lombardi, P. Antonini *et al.*, Laramed: A laboratory for radioisotopes of medical interest, Molecules **24**, 20 (2019).

[10] F. F. Knapp and A. Dash, *Radiopharmaceuticals for Therapy* (Springer, New York, 2016).

[11] *Cyclotron Produced Radionuclides: Physical Characteristics and Production Methods*, Technical Reports Series Vol. 468 (International Atomic Energy Agency, Vienna, 2009).

[12] L. De Nardo, G. Pupillo, L. Mou, D. Furlanetto, A. Rosato, J. Esposito, and L. Meléndez-Alafort, Preliminary dosimetric analysis of dota-folate radiopharmaceutical radiolabelled with ^{47}Sc produced through natv (p, x) ^{47}Sc cyclotron irradiation, Phys. Med. Biol. **66**, 025003 (2021).

[13] C. G. Heininger and E. O. Wiig, Spallation of vanadium with 60-, 100-, 175-, and 240-mev protons, Phys. Rev. **101**, 1074 (1956).

[14] N. Otuka *et al.*, Towards a more complete and accurate experimental nuclear reaction data library (EXFOR): International collaboration between Nuclear Reaction Data Centres (NRDC), Nucl. Data Sheets **120**, 272 (2014).

[15] S. Hontzeas and L. Yaffe, Interaction of vanadium with protons of energies up to 84 mev, Can. J. Chem. **41**, 2194 (1963).

[16] R. Michel, G. Brinkmann, H. Weigel, and W. Herr, Measurement and hybrid-model analysis of proton-induced reactions with V, Fe and Co, Nucl. Phys. A **322**, 40 (1979).

[17] R. Michel, F. Peiffer, and R. Stück, Measurement and hybrid model analysis of integral excitation functions for proton-induced reactions on vanadium, manganese and cobalt up to 200 mev, Nucl. Phys. A **441**, 617 (1985).

[18] V. N. Levkovskij, *Cross-Section of Medium Mass Nuclide Activation (A = 40–100) by Medium Energy Protons and Alpha-Particles (E = 10–50 MeV)* (Inter-Vesi, Moscow, 1991).

[19] F. Ditrói, F. Tárkányi, S. Takács, and A. Hermanne, Activation cross-sections of proton induced reactions on vanadium in the 37–65 mev energy range, Nucl. Instrum. Methods Phys. Res., Sect. B **381**, 16 (2016).

[20] L. Canton and A. Fontana, Nuclear physics applied to the production of innovative radiopharmaceuticals, Eur. Phys. J. Plus **135**, 770 (2020).

[21] A. Gilbert and A. G. W. Cameron, A composite nuclear-level density formula with shell corrections, Can. J. Phys. **43**, 1446 (1965).

[22] A. V. Ignatyuk, J. L. Weil, S. Raman, and S. Kahane, Density of discrete levels in ^{116}Sn, Phys. Rev. C **47**, 1504 (1993).

[23] P. Demetriou and S. Goriely, Microscopic nuclear level densities for practical applications, Nucl. Phys. A **695**, 95 (2001).

[24] F. Minato, Nuclear level densities with microscopic statistical method using a consistent residual interaction, J. Nucl. Sci. Technol. **48**, 984 (2011).

[25] S. Hilaire and S. Goriely, Global microscopic nuclear level densities within the HFB plus combinatorial method for practical applications, Nucl. Phys. A **779**, 63 (2006).

[26] S. Goriely, S. Hilaire, and A. J. Koning, Improved microscopic nuclear level densities within the Hartree-Fock-Bogoliubov plus combinatorial method, Phys. Rev. C **78**, 064307 (2008).

[27] M. Hillman and J. R. Grover, Shell-model combinatorial calculations of nuclear level densities, Phys. Rev. **185**, 1303 (1969).

[28] S. Hilaire, M. Girod, S. Goriely, and A. J. Koning, Temperature-dependent combinatorial level densities with the D1M Gogny force, Phys. Rev. C **86**, 064317 (2012).

[29] G. Pupillo, L. Mou, F. Haddad, A. Fontana, and L. Canton, New results on the ^{nat}V(p, x) ^{43}Sc cross section: Analysis of the discrepancy with previous data, Nucl. Instrum. Methods Phys. Res., Sect. B **464**, 32 (2020).

[30] F. Haddad, L. Ferrer, A. Guertin, T. Carlier, N. Michel, J. Barbet, and J.-F. Chatal, Arronax, a high-energy and high-intensity cyclotron for nuclear medicine, Eur. J. Nucl. Med. Mol. Imaging **35**, 1377 (2008).

[31] IAEA Monitor Reactions (2017), https://www-nds.iaea.org/medical/monitor_reactions.html, accessed March 2019.

[32] J. F. Ziegler, M. D. Ziegler, and J. P. Biersack, SRIM: The stopping and range of ions in matter (2010), Nucl. Instrum. Methods Phys. Res., Sect. B **268**, 1818 (2010).

[33] N. Otuka, B. Lalremruata, M. Khandaker, A. Usman, and L. Punte, Uncertainty propagation in activation cross section measurements, Radiat. Phys. Chem. **140**, 502 (2017).

[34] S. Goriely, S. Hilaire, and A. J. Koning, Improved predictions of nuclear reaction rates with the TALYS reaction code for astrophysical applications, Astron. Astrophys. **487**, 767 (2008).

[35] S. Hilaire, A. J. Koning, and S. Goriely, Microscopic cross sections: An utopia?, EPJ Web Conf. **8**, 02004 (2010).

[36] E. Bauge, J. P. Delaroche, and M. Girod, Lane-consistent, semimicroscopic nucleon-nucleus optical model, Phys. Rev. C **63**, 024607 (2001).

[37] H. A. Bethe, An attempt to calculate the number of energy levels of a heavy nucleus, Phys. Rev. **50**, 332 (1936).

[38] V. Zelevinsky and M. Horoi, Nuclear level density, thermalization, chaos, and collectivity, Prog. Part. Nucl. Phys. **105**, 180 (2019).

[39] S. M. Grimes, Nuclear level densities, J. Nucl. Sci. Technol. **39**, 709 (2002).

[40] R. Capote, M. Herman, P. Obložinský, P. G. Young, S. Goriely, T. Belgya, A. V. Ignatyuk, A. J. Koning, S. Hilaire, V. A. Plujko *et al.*, RIPL: Reference Input Parameter Library for Calculation of Nuclear Reactions and Nuclear Data Evaluations, Nucl. Data Sheets **110**, 3107 (2009).

[41] J. P. Jeukenne, A. Lejeune, and C. Mahaux, Microscopic calculation of the symmetry and coulomb components of the complex optical-model potential, Phys. Rev. C **15**, 10 (1977).

[42] J. P. Jeukenne, A. Lejeune, and C. Mahaux, Optical-model potential in finite nuclei from reid's hard core interaction, Phys. Rev. C **16**, 80 (1977).

[43] S. Grimes, J. Anderson, A. Kerman, and C. Wong, Role of isospin in statistical processes, Phys. Rev. C **5**, 85 (1972).

[44] C. Lux, N. Porile, and S. Grimes, Isospin mixing in in 111 and the inclusion of additional terms in the mixing formalism, Phys. Rev. C **15**, 1308 (1977).

[45] A. J. Koning, S. Hilaire, and S. Goriely, Global and local level density models, Nucl. Phys A **810**, 13 (2008).

[46] A. Koning, S. Hilaire, and S. Goriely, TALYS-1.9 User Manual, http://www.talys.eu.

[47] F. James and M. Roos, Minuit: A system for function minimization and analysis of the parameter errors and corrections, Comput. Phys. Commun. **10**, 343 (1975).

[48] F. Tárkányi, A. Ignatyuk, A. Hermanne, R. Capote, B. Carlson, J. W. Engle, M. A. Kellett, T. Kibedi, G. Kim, F. Kondev *et al.*, Recommended nuclear data for medical radioisotope production: Diagnostic gamma emitters, J. Radiol. Nucl. Chem. **319**, 487 (2019).

[49] A. Yu. Konobeyev, U. Fischer, P. E. Pereslavtsev, and A. J. Koning, Implementation of GDH model in TALYS-1.7 code, KIT Scientific Working Papers Report No. 45, 2016, https://publikationen.bibliothek.kit.edu/1000090132/22033694.

[50] M. Blann, Importance of the Nuclear Density Distribution on Pre-Equilibrium Decay, Phys. Rev. Lett. **28**, 757 (1972).

[51] M. Blann and H. K. Vonach, Global test of modified precompound decay models, Phys. Rev. C **28**, 1475 (1983).

[52] C. H. M. Broeders, A. Yu. Konobeyev, A. Yu. Korovin, V. P. Lunev, and M. Blann, ALICE/ASH: Pre-compound and evaporation model code system for calculation of excitation functions, energy and angular distributions of emitted particles in nuclear reactions at intermediate energies, FZKA Report No. 7183, 2006, https://publikationen.bibliothek.kit.edu/270064701.

[53] T. Böhlen, F. Cerutti, M. Chin, A. Fassò, A. Ferrari, P. Ortega, A. Mairani, P. Sala, G. Smirnov, and V. Vlachoudis, The fluka code: Developments and challenges for high energy and medical applications, Nucl. Data Sheets **120**, 211 (2014).

[54] A. Ferrari, J. Ranft, P. R. Sala, and A. Fassò, FLUKA: A multi-particle transport code, program version 2005, CERN Report No. 2005-10, 2005, 10.5170/CERN-2005-010.

[55] Medical Isotope Browser, https://www-nds.iaea.org/relnsd/isotopia/isotopia.html, accessed May 2021.

[56] J. W. Engle, A. V. Ignatyuk, R. Capote, B. Carlson, A. Hermanne, M. A. Kellett, T. Kibedi, G. Kim, F. G. Kondev, M. Hussain *et al.*, Recommended nuclear data for the production of selected therapeutic radionuclides, Nucl. Data Sheets **155**, 56 (2019).